The pathophysiological mechanism of kidney injury caused by *Beni-koji Choleste-Help*/puberulic acid is proximal tubular mitochondrial dysfunction

Yuta Sekiguchi[1], Makiko Mori[1], Haruka Maruyama[1,2], Yuki Nakao[1], Hiroaki Kikuchi[1], Shintaro Mandai[1], Fumiaki Ando[1], Koichiro Susa[1], Takayasu Mori[1], Yuma Waseda[3], Soichiro Yoshida[3], Yasuhisa Fujii[3], Wakana Shoda[4], Daiei Takahashi[4], Rei Okazaki[5], Kenji Ikeda[5], Tetsuya Yamada[5], Eisei Sohara[1], Shinichi Uchida[1], Yutaro Mori[1]

[1]Department of Nephrology, [3]Department of Urology and [5]Department of Molecular Endocrinology and Metabolism, Graduate School of Medical and Dental Sciences, Institute of Science Tokyo, Tokyo 113-8510, Japan.

[2]Kidney Disease and Transplant Center, Shonan Kamakura General Hospital, Kamakura 247-8533, Japan

[4]Department of Nephrology, Japanese Red Cross Musashino Hospital, Tokyo 180-0023, Japan.

Lead contact and Corresponding author:

Yutaro Mori, MD, PhD

Department of Nephrology

Graduate School of Medical and Dental Sciences

Institute of Science Tokyo

1-5-45, Yushima, Bunkyo-ku, Tokyo 113-8510, Japan

Phone: +81-3-5803-5214; Fax: +81-3-5803-5215; Email: y-mori.kid@tmd.ac.jp

Abstract

Introduction: In March 2024, kidney injury sometimes accompanied with Fanconi syndrome caused by a supplement made from red yeast rice (*Beni-koji Choleste-Help*) were reported in Japan. By November 24, 2024, 2,628 people had visited medical facilities, resulting in a social problem. Many patients still have a decline in eGFR. The previous report, however, did not indicate anything other than that puberulic acid which newly identified nephrotoxicity was contained in toxic lots. The pathophysiology of those nephropathies should be determined. Here, we discovered that mitochondrial dysfunction in renal proximal tubular epithelial cells plays a pivotal role in the nephrotoxicity.

Methods: To assess the effects of *Choleste-Help* and puberulic acid, we performed RNA-seq, extracellular flux analysis (Seahorse XF Analyzer), immunofluorescence staining, Western blotting, and other complementary assays across multiple experimental models, including human kidney biopsy specimens, human-derived primary renal proximal tubular epithelial cells (hRPTECs), human renal organoids, and mice.

Results: A patient renal biopsy sample showed Kidney Injury Molecule-1 (KIM-1) expression in proximal tubules surrounded by activated myofibroblasts, indicating acute tubular damage and interstitial fibrosis associated with injured tubules. Mice treated with the toxic lot of *Choleste-Help* and puberulic acid showed kidney injury with Fanconi syndrome-like urinary findings. Pathological sections showed tubular necrosis and interstitial fibrosis. RNA-seq on whole kidneys of those mice presented the renal damage caused by *Choleste-Help* and puberulic acid produced similar RNA patterns, indicating puberulic acid is a causative agent. Gene Ontology (GO) analysis comparing the normal and toxic lot revealed downregulation of mitochondrial-related pathways. Puberulic acid also showed toxicity on hRPTECs and tubular

organoids. *In vitro* experiments with hRPTECs revealed that it causes mitochondrial damage especially on mitochondrial respiratory chain at first and leads to cell death, mainly necrosis. Conclusion: puberulic and a toxic lot of *Choleste-Help* cause direct mitochondrial damage on tubular epithelial cells, followed by necrosis.

Keywords

Acute kidney injury, organoid, tubuloid, puberulic acid, Fanconi syndrome

Graphical Abstract

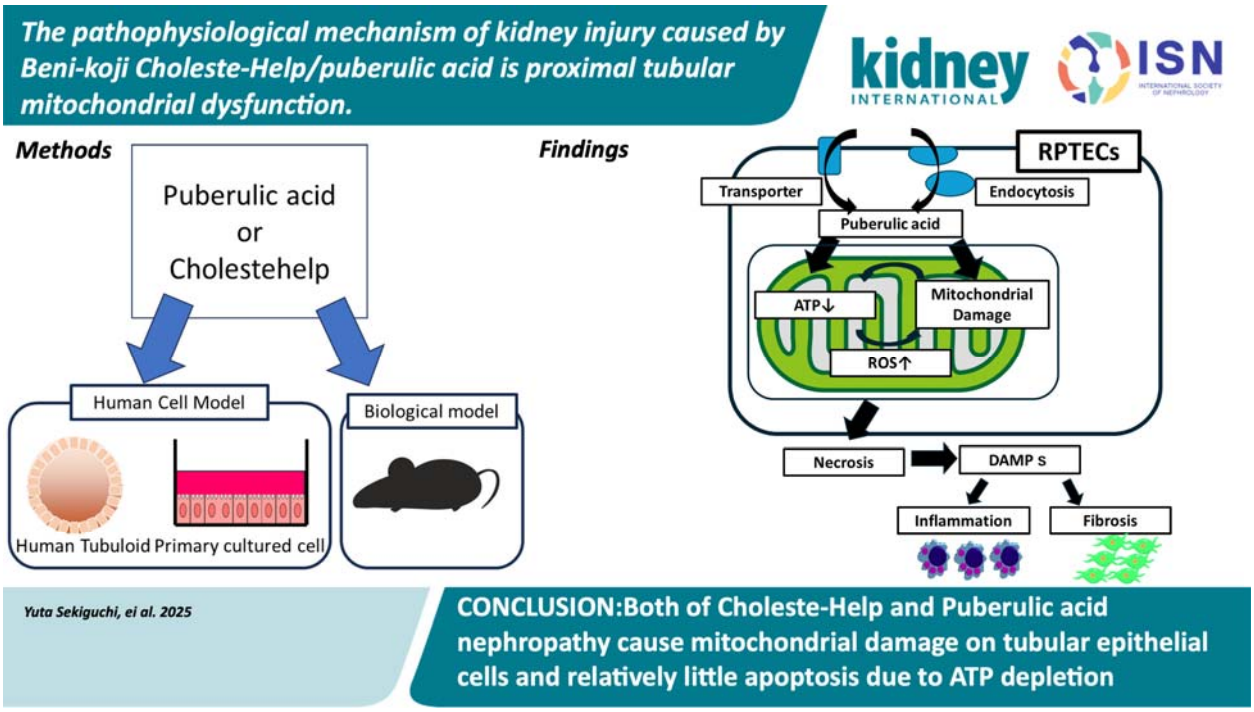

Translational Statement

Our research revealed the pathophysiology of puberulic acid nephropathy, which suffers many patients. And we used not only animal models, but human kidney-derived primary cultured tubular epithelial cells and its 3D organoids, which are ones of the closest models of the human body.

Introduction

In recent years, due to growing health consciousness, supplements and herbal medicines are widely used. However, these often produce side effects.[1,2] From the second half of 2023 to 2024, a serious health issue arose in Japan. Multiple cases of kidney dysfunction associated with Benikoji tablets were reported, prompting Kobayashi Pharmaceutical Co., Ltd. to implement a voluntary recall on March 22, 2024.[3] The supplement most taken by patients was *Beni-koji Choleste-Help* (*Choleste-Help*). As reported by Ministry of Health, Labour and Welfare in Japan, 1,961 people consulted with doctor and 348 people was hospitalized due to renal injury after taking *Beni-koji supplements*.[3] The social significance of this study is extremely high. This supplement, which contains Monascus-derived red yeast[4] and a compound structurally similar to the cholesterol-lowering drug lovastatin, was marketed as achieving similar effects at lower concentrations.[5] Patients who took these supplements developed acute kidney injury, proteinuria, and Fanconi syndrome[6-8], and many patients still had CKD-level kidney damage 120 days after starting treatment.[9] A compound called puberulic acid and two other new compounds were identified as causative substances, and puberulic acid is the most likely causative substance[10,11], but only little information[12,13] are available at this time. Puberulic acid was originally developed as an antimalarial agent; however, its development was discontinued due to lethality observed in mice at high doses, the cause of which remains unknown.[14] Aristolochic acid, the most widely known kidney-toxic substance derived from traditional Chinese medicine, is known not only to cause tubular damage, but also to induce CKD and increase the incidence of cancer[15-17]. Therefore, it is necessary to collect various information on this new toxic substance, including its damaged pathways. We have succeeded in identifying the main pathways of damage to the kidneys caused by this substance from a basic medical perspective, as we describe in this report.

To the best of our knowledge, this is the first study to demonstrate the toxicity of puberulic acid in human cells.

Methods

Immunostaining of human renal biopsy samples

Written informed consent was obtained by the patient of *Choleste-Help* nephropathy for publishing reports regarding renal biopsy and other clinical information. After deparaffinization with xylene, antigen retrieval was performed by heat-induced epitope retrieval using boiling in Antigen Unmasking Solution (Citric Acid base, H-3300, Vector Laboratories Inc.). Sections were incubated with a goat anti-KIM-1 antibody (1:200, AF1750, R&D Systems, MN, USA) and a rabbit anti-α-smooth muscle actin (α-SMA) antibody conjugated with Cy3 (1:400, C6198, Sigma-Aldrich). For the detection of KIM-1, an Alexa Fluor 488-conjugated donkey anti-goat IgG secondary antibody (1:500, A11055 Thermo Fisher Scientific) was used.

Animal treatment and tissue collection

Eight-week-old male C57BL/6J mice were used for all experiments. Mice were randomly assigned to four groups (n = 6-10 per group): (1) control (PBS), (2) *Choleste-Help* normal batch (1,000 mg/day), (3) *Choleste-Help* toxic batch (1,000 mg/day), and (4) puberulic acid (1 mg/day). Treatments were administered either by oral gavage or intraperitoneal injection for six consecutive days, followed by a one-day rest period. On day 7, mice were euthanized, and bloods, urines, and whole kidneys were rapidly harvested, snap-frozen in liquid nitrogen, and stored at −80°C until RNA extraction. Hematological and urinary analyses were outsourced and performed by Oriental Yeast Co., Ltd.

Histological Preparation and Staining

Hematoxylin and eosin (H&E) staining was outsourced to the Research Core Center of Institute of Science Tokyo. Masson's trichrome staining was performed using a standard protocol. For each sample, one kidney section was selected to reduce non-specific blue staining. Whole images of the sections were acquired, and the fibrotic area, indicated by blue staining, was quantified using Image J Fiji (https://imagej.net/software/fiji/downloads). The percentage of the blue-stained area relative to the total kidney section area was calculated for each sample.

RNA-seq and analysis

Mouse whole kidney total RNA was extracted using Sepasol (Nacalai Tesque, Japan) and purified with Direct-zol RNA Miniprep Plus Kit (Zymo Research, R2070). Samples (n = 5, each) with RIN > 7.5 were processed by ReRexa Inc. using NEBNext kits and sequenced on NovaSeq X Plus (2 × 150 bp, ~ 40 million reads/sample). Reads were trimmed with fastp and quantified with Salmon (GENCODE vM33). DEGs were identified using DESeq2 (padj < 0.05, |log2FC| > 1, baseMean > 10). PCA and heatmaps were generated in RStudio (Windows), with Salmon outputs from WSL2. The details of experimental methods for RNA-seq analysis are described in **Supplementary Methods**.

Cell culture experiment

Human kidney samples were collected from patients undergoing clinically indicated nephrectomy at the Institute of Science Tokyo Hospital in Tokyo, Japan. The protocol was approved by the Institutional Review Board of the Ethics Committee of Institute of Science Tokyo (M2022-005). Primary human renal proximal tubular epithelial cells (hRPTECs) were isolated from unaffected areas of kidneys removed during nephrectomy procedures performed on

patients with renal cell carcinoma or urinary tract malignancies by modifying a previously established protocol.[18,19] Briefly, the isolation procedure involved mincing the human renal cortex and then digesting it in a solution of Collagenase type II (1.0 mg/mL) (Worthington Biochemical, NJ, USA). The enzyme reaction was terminated with fetal bovine serum (FBS), and the samples were resuspended in hRPTECs culture medium containing DMEM/F-12 (Nacalai Tesque, Kyoto, Japan), with BSA (Nacalai Tesque), Antibiotic–Antimycotic (ThermoFisher Scientific, MA, USA), hydrocortisone (ThermoFisher Scientific, MA, USA), ITS liquid media supplement (Sigma-Aldrich, MO, USA), and human recombinant epidermal growth factor (EGF) (ThermoFisher Scientific, MA, USA).

Human renal tubuloids culture

hRPTECs were seeded onto ultralow attachment plates at a density of 5.0×10^5 cells/well using Advanced RPMI 1640 medium (ThermoFisher Scientific), supplemented with 5% FBS. After a 2–3-day incubation period, Matrigel (Corning, NY, USA) was added to stimulate tubuloid formation. The following day, the culture medium was changed to Advanced RPMI 1640 medium with 5% FBS, EGF, FGF2, and HGF (tubuloids media). Media was changed three times in a week to maintain optimal cell growth conditions. Tubuloids were usually ready for experimentation within 1–2 weeks of starting the culture.

Western blot analysis

The samples were lysed, and the protein was purified by using a lysis buffer [50 mM Tris-HCl (pH 7.5), 150 mM NaCl, 1% Nonidet P-40, 1 mM sodium orthovanadate, 50 mM sodium fluoride, and protease inhibitor cocktail]. Since the protein content of the Tuburoids was low,

four wells under the same conditions were combined into a single sample. Proteins were separated by 10% SDS-PAGE and transferred onto a nitrocellulose membrane. Protein bands were visualized using Western Blue (Promega, WI, USA). Rabbit anti–ERK1/2 (p44/42 MAPK) antibody (9102S, Cell Signaling Technology) (1:1000) or rabbit anti-beta actin antibody (4967S, Cell Signaling Technology) (1:1000) was used as a loading control. Primary antibodies were also used, such as rabbit anti-KIM-1 polyclonal antibody (PA5-79345, Thermo Fisher Scientific) (1:1000), rabbit anti Phospho-Histone H2AX (Ser139) antibody (9718S, Cell Signaling Technology) (1:1000). As secondary antibody**,** anti-rabbit IgG alkaline phosphatase–conjugated secondary antibody (S373B, Promega) was used. Densitometry was performed by using Image J Fiji.

Cell viability assay

hRPTECs were seeded at a density of 2×10^4 cells per well in 96-well plates. After reaching confluence in two days post-passaging, cells were treated with the indicated compound for 48 hours. Cell viability was assessed using Cell Count Reagent SF (Nacalai Tesque, #07553) according to the manufacturer's instructions. Cells were incubated with the reagent (10% v/v) at 37 °C for 1 hour. Absorbance was measured at 450 nm using a microplate reader (FilterMax F5, Molecular Devices). Cell viability was expressed as a percentage of absorbance relative to vehicle control. The EC value was estimated using a four-parameter logistic model fitted to the viability data. Due to data sparsity at higher concentrations, the confidence intervals could not be fully resolved. Therefore, the EC value should be interpreted with caution.

Annexin V assay and flow cytometry

hRPTECs were seeded at a density of 5 × 10□ cells per well in 12-well plates. After reaching confluence in two days post-passaging, cells were treated with the indicated compound for 48 hours. Following treatment, 1 × 10□ cells were collected and stained using the Annexin V Apoptosis Detection Kit (Nacalai Tesque, product number 15342-54) according to the manufacturer's instructions. Flow cytometric analysis was performed using a FACS Lyric™ system (BD Biosciences). Data was analyzed with FlowJo software (BD Biosciences), and cell populations were classified into live, early apoptotic, and late apoptotic/necrotic based on Annexin V and propidium iodide (PI) staining patterns.

JC-1 staining

hRPTECs were seeded at a density of 5 × 10□ cells per well in 12-well plates. In three days, post-passaging, cells were treated with the indicated compound for 18 or 24 hours. Then, mitochondrial membrane potential was assessed using the JC-1 dye (T3168, Thermo Fisher Scientific) according to the manufacturer's instructions. Briefly, cells were incubated with 1.5□μM JC-1 in culture medium at 37□°C for 20□minutes. After incubation, cells were washed twice with PBS and analyzed by confocal microscopy (Eclipse Ti2 from Nikon, excitation/emission: 488/530□nm for green monomers, 540/590□nm for red aggregates), with the NIS-Elements Advanced Research microscope system serving as the operating system. Fluorescence images were analyzed using ImageJ Fiji. For each well, three fields of view were randomly selected, and the entire field area was defined as the region of interest (ROI). The red-to-green fluorescence ratio was calculated to assess mitochondrial membrane potential.

ATP measurement

hRPTECs were seeded at a density of 2×10^4 cells per well in 96-well plates. After reaching confluence in two days post-passaging, cells were treated with the indicated compound for 6, 24 or 48 hours. Cellular ATP levels were quantified using the CellTiter-Glo® 2.0 Cell Viability Assay (Promega, Madison, WI, USA) according to the manufacturer's instructions. Luminescence was measured using a Varioskan™ LUX Multimode Microplate Reader (Thermo Fisher Scientific, Waltham, MA, USA). The luminescence intensity, which is proportional to the amount of ATP, was recorded and normalized to control samples.

Seahorse XF Cell Mito Stress Test

Mitochondrial respiratory function was assessed using the Seahorse XF Cell Mito Stress Test (Agilent Technologies) following the manufacturer's protocol. hRPTECs were seeded into Seahorse XF96 Cell Culture Microplates at a density of 40,000 cells/well and cultured 4 days. Cells were treated with puberulic acid (100 μM) for 4.5 or 9 hours, while untreated cells served as the control group. Prior to the assay, the culture medium was replaced with Seahorse XF assay medium (non-buffered DMEM supplemented with 10 mM glucose, 1 mM pyruvate, and 2 mM glutamine; pH 7.4) and incubated for 1 hour at 37°C in a non-CO□ incubator for equilibration. The assay was performed using a Seahorse XFe96 Analyzer, and the following compounds were sequentially injected: oligomycin (1.5 μM) to inhibit ATP synthase, FCCP (4 μM) to uncouple the mitochondrial membrane potential and determine maximal respiration, and rotenone (0.5 μM) plus antimycin A (0.5 μM) to inhibit complex I and III, respectively, thereby determining non-mitochondrial respiration. Oxygen consumption rate (OCR) was measured at baseline and following each injection. Key parameters including basal respiration, ATP-linked respiration, maximal respiration, spare respiratory capacity, and proton leak were calculated using Wave

software (Agilent). All measurements were conducted in technical replicates (n = 6 wells per group), and background correction was applied based on cell-free wells.

Quantification and statistical analyses

Figure Legends indicate the number of samples assayed in each experiment. One-way ANOVA was used for general comparisons. When data were normalized to the control group mean, Welch's ANOVA was applied. When each value was individually normalized to its corresponding control, the Kruskal–Wallis test was used. A p-value < 0.05 was considered statistically significant. Statistical significance was indicated by asterisks as follows: * $p < 0.05$, ** $p < 0.01$, *** $p < 0.001$, **** $p < 0.0001$. All statistical analyses were performed with GraphPad Prism by GraphPad Software Inc. (San Diego, CA, USA). To minimize the influence of aberrant values, extreme outliers defined as having Z-scores greater than 2 were excluded from the analysis as necessary.

Study approval

The protocol for human kidney samples for primary culture and the one for analyzing human kidney biopsy samples were approved by the Institutional Review Board of the Ethics Committee of Institute of Science Tokyo (M2022-005, I2024-097) and conducted in accordance with the regulations of the ethics committee of Kidney Disease and Transplant Center, Shonan Kamakura General Hospital. Animal experiments were approved by the Animal Care and Use Committee of Institute of Science Tokyo (A2023-109C3) according to the animal experiment guidelines of the Japan Ministry of Education, Culture, Sports, Science and Technology.

Results

A human kidney biopsy sample of a *Choleste-Help* patient show KIM-1 positive proximal tubular epithelial cells surrounded by α-SMA positive cells

Renal biopsy samples obtained from a patient who visited our affiliated hospital revealed marked tubular dilatation and detachment of tubular epithelial cells and tubular casts were observed in the lumen of the renal tubules (**Figure 1a**), whose case we reported recently.[7] Immunostaining demonstrated the presence of KIM-1–positive tubular epithelial cells, an established marker of tubular injury,[20] along with surrounding expression of α-SMA, indicative of early fibrotic changes associated with tubular epithelial damage (**Figure 1b**). Although the degree of renal injury in this case was relatively mild, the findings suggest the presence of fibrosis at an early stage.

Wild type mice showed acute kidney failure and Fanconi-like phenotype by *Choleste-Help* toxic lot and puberulic acid

To investigate the *in vivo* toxicity and underlying mechanisms, we administered *Choleste-Help* (normal lot and toxic lot), the suspected causative compound puberulic acid, and vehicle (PBS) to mice once daily for six days. Following a one-day drug holiday, the mice were sacrificed on day 7 (**Figure 2a, Supplementary Figure 1**).

In both the *Choleste-Help* toxic lot and puberulic acid groups, serum biochemical analysis revealed elevated blood urea nitrogen (BUN) and creatinine (Cr) levels (**Figure 2b**). Urinalysis showed increased urinary albumin-to-creatinine (Alb/Cr), glucose-to-creatinine (Glu/Cr), and N-acetyl-β-D-glucosaminidase-to-creatinine (NAG/Cr) ratios, which is consistent not only with tubular injury but also with Fanconi syndrome. These findings indicate that both

compounds induce proximal tubular injury, renal dysfunction, proteinuria, and a Fanconi syndrome-like phenotype in mice, recapitulating features observed in human cases.

Histological examination using hematoxylin and eosin (HE) staining revealed tubular dilatation and epithelial cell detachment (**Figure 2c**), consistent with human biopsy findings. In addition, intratubular casts—also observed in human sample—were present in treated mice. Furthermore, Masson's Trichrome staining demonstrated a significant increase in fibrotic areas in both the *Choleste-Help* toxic lot and puberulic acid groups (**Figure 2d**). These results suggest that *Choleste-Help* toxic lot and puberulic acid can induce renal fibrosis at an early stage *in vivo*.

Mice treated with *Choleste-Help* toxic lot and puberulic acid exhibited highly similar gene expression profiles, as revealed by RNA-seq analysis

We performed bulk RNA sequencing (RNA-seq) using whole-kidney samples (n = 5 for each sample) from the experimental groups as a transcriptomic analysis. Principal component analysis (PCA) and hierarchical clustering (**Figure 3a, b**) demonstrated that the *Choleste-Help* toxic lot and puberulic acid groups clustered closely together, indicating a high degree of similarity in their transcriptomic responses.

To assess the overall transcriptomic changes and data quality, a volcano plot, generated to compare gene expression between toxic lot vs normal lot and, and heatmap were generated (**Figure 3c, d, Supplementary Figure 2**). These visualizations illustrate the global expression landscape and support the reliability and robustness of the dataset. In the Volcano plot, Spp1 and Havcr1 were among the top upregulated genes, supporting the validity of the model as a representation of kidney injury.

Correlation analysis between differential gene expression profiles revealed a strong correlation (Pearson's r = 0.736) between the comparisons of *Choleste-Help* toxic lot vs. normal lot and puberulic acid vs. PBS (**Figure 3e**). Moreover, more than 70% of differentially expressed genes (DEGs) overlapped between the two comparisons, suggesting that the toxic responses induced by *Choleste-Help* toxic lot and puberulic acid are highly similar at the transcriptomic level (**Figure 3f**).

Although the precise concentration of puberulic acid contained in *Choleste-Help* is unknown and not equivalent to the dose used in the isolated puberulic acid group, the similarity in gene expression patterns strongly suggests that puberulic acid is likely a major contributor to the nephrotoxicity observed in *Choleste-Help* toxic lot.

Mitochondrial function was significantly suppressed indicated by comprehensive transcriptomic analysis with RNA-seq

We performed Gene Ontology (GO) enrichment analysis based on the comparison between the *Choleste-Help* toxic lot and the normal lot. Based on the GO cellular component (CC) analysis using the absolute value of log2 fold change, Among the top 10 downregulated GO terms in the Cellular Component category (**Figure 4a**), many were related to mitochondria, indicating that mitochondria was one of the most severely affected organelles. GO terms associated with upregulated genes were shown in **Supplementary Figure 3a**. Notably, all mitochondrial-related terms showed a trend toward downregulation. Furthermore, in the GO biological process (BP) analysis, the top 10 downregulated pathways were predominantly associated with mitochondrial function (**Figure 4b**). GO terms associated with upregulated genes are shown in **Supplementary Figure 3b**.

In addition, GO analysis of the “molecular function” category revealed downregulation of various transporter activities, supporting the hypothesis that this compound induces a renal injury pattern consistent with Fanconi syndrome (**Figure 4c**). GO terms associated with upregulated genes are shown in **Supplementary Figure 3c**, results of the GSEA and KEGG pathway analyses are presented in **Supplementary Figures 4 and 5**, respectively.

Puberulic acid exhibited approximately half the cytotoxicity of cisplatin in hRPTECs and kidney injury marker KIM-1 and DNA damage marker γH2AX were upregulated following puberulic acid exposure

To evaluate the potential nephrotoxicity of puberulic acid in humans, we exposed primary cultured hRPTECs to puberulic acid for 48 hours and assessed cytotoxicity using a cell viability assay. Cisplatin was included as a positive control under the same conditions. Puberulic acid exhibited dose-dependent toxicity, with an EC□□ of 66.04 μM, approximately twice that of cisplatin (EC□□ = 31.24 μM), indicating moderate cytotoxicity relative to cisplatin (**Figure 5a**).

We further examined the effects of puberulic acid using both conventional 2D cultures and 3D-cultured renal tubuloids derived from hRPTECs. Puberulic acid was administered at 48-hour intervals for a total of three exposures. Western blot analysis revealed increased expression of the kidney injury marker KIM-1 in tubuloids and the DNA damage marker γH2AX in both models following treatment (**Figure 5b, c**). Notably, the tubuloids responded to puberulic *acid* at approximately one-tenth the concentration required in the 2D cultures, indicating higher sensitivity in the 3D system.

DNA damage and its response are known to be associated with cellular senescence through cell cycle arrest[21]. The senescence-associated secretory phenotype (SASP) is considered

a driver of chronic fibrosis progression.[22,23] In mouse RNA-seq data, Cdkn1a expression was markedly upregulated, whereas Cdkn2a showed only a modest increase (**Supplementary Figure 6a**). Furthermore, in the *in vitro* model with a 6-day exposure, no induction of p16 expression was observed (**Supplementary Figure 6b**). These findings suggest that cell cycle arrest induced by puberulic acid occurs without clear evidence of cellular senescence.

Annexin V assay revealed that necrosis accounted for most of the cell death

To evaluate the involvement of apoptosis, we performed live-cell immunostaining using Annexin V and propidium iodide (PI), followed by flow cytometric analysis. As a positive control, cells were treated with cisplatin, and the types of cell death were assessed at 48 hours post-treatment.

The results showed that, under conditions with comparable numbers of viable cells, the proportion of apoptotic cells in the puberulic acid–treated group was approximately half that observed in the cisplatin-treated group, indicating a relatively low level of apoptosis (**Figure 6a**). Furthermore, at earlier points (24 and 40 hours), the proportion of apoptotic cells in the puberulic acid group was even lower (**Figure 6b**).

These findings suggest that while puberulic acid does induce apoptosis, it occurs at relatively low levels. This observation is consistent with the renal biopsy findings in human cases, where necrosis was the predominant histological feature.

We also examined other forms of cell death, including necroptosis and pyroptosis (**Supplementary Figure 7**); however, in our *in vitro* experiments, we did not observe upregulation of pathway-specific molecules at the protein level, suggesting that necroptosis and pyroptosis are not involved in puberulic acid-induced cell death.

In addition, at the 24-hour time point, exposure to 100 μM puberulic acid induced only minimal cell death. Therefore, analyzing cells prior to this time point may provide further insights into the upstream mechanisms responsible for puberulic acid–induced cytotoxicity.

JC-1 staining and measuring of ATP revealed a decrease in mitochondrial membrane potential and ATP depletion preceding the onset of cell death

JC-1 staining was performed at 18- and 24-hours following treatment with 100 μM puberulic acid—time points at which minimal cell death was observed (**Figure 7a**). At 18 hours, a reduction in red fluorescence, indicative of healthy mitochondria, was already evident, accompanied by an increase in green fluorescence, reflecting a loss of mitochondrial membrane potential. This trend became more pronounced at 24 hours.

These findings indicate that mitochondrial dysfunction occurs prior to the onset of cell death following puberulic acid exposure. Thus, puberulic acid–induced mitochondrial damage is likely one of the primary causes of its cytotoxic effects.

In addition, ATP measurement using a luminescence-based assay revealed a reduction as early as 6 hours after treatment (**Figure 7b**). This suggests that puberulic acid impairs ATP production, likely through disruption of the mitochondrial respiratory chain.

Seahorse assay revealed that puberulic acid cause reduction in maximal mitochondrial respiration

To evaluate the impact of puberulic acid (100 μM) on mitochondrial respiration, we conducted a Seahorse XF Cell Mito Stress Test and monitored the oxygen consumption rate (OCR) in control and treated cells (4.5 h and 9 h post-exposure). Puberulic acid exposure resulted in a

time-dependent suppression of mitochondrial respiration (**Figure 8a**). The maximal respiration (after FCCP injection) was significantly lower in the 9 h treatment group compared to both the 4.5 h treatment and control groups, suggesting a progressive impairment in the mitochondrial electron transport chain capacity. These results indicate that puberulic acid induces a progressive decline in mitochondrial respiratory function, potentially through cumulative damage to the oxidative phosphorylation machinery. A significant difference was also observed in ECAR at its peak following oligomycin injection (**Figure 8b**), indicating a compensatory upregulation of glycolysis.

Discussion

In this study, we demonstrated that *Choleste-Help* and puberulic acid induce highly similar patterns of renal injury at the transcriptomic level in mice. Importantly, we identified mitochondrial dysfunction especially on mitochondrial respiratory chain as one of the key mechanisms contributing to puberulic acid induced cell death in hRPTECs. We observed acute renal fibrosis in mouse models treated with puberulic acid or the toxic lot of *Choleste-Help*, as well as in human patients. This was supported by increased fibrotic areas on Masson's trichrome staining and upregulation of fibrosis-related markers in RNA-seq analysis (**Supplementary Figure 8, 9**). We also found out proximal tubular epithelial cell death after puberulic acid treatment[7,9] in a relatively short period, which was mainly necrosis. In the status of proximal tubular epithelial necrosis, Damage-Associated Molecular Patterns (DAMPs) are released from dead cell bodies, resulting in myofibroblast activation and/or immune cell infiltration.[24,25] This may explain the early onset of fibrosis observed in our model.

Mitochondrial damage was demonstrated by early reductions in ATP levels and JC-1 signals prior to cell death in hRPTECs, which was supported by RNA-seq data in mice treated with puberulic acid or *Choleste-Help* toxic lot. In addition, a marked reduction in mitochondria in electron micrographs of kidneys from mice treated with puberulic acid was reported in a preprint,[12] which is consistent with our findings. Since apoptosis is an ATP-dependent process,[26,27] it is well known that necrosis tends to be predominant under conditions of ATP depletion.[28,29] Therefore, we speculate that the primary mitochondrial damage led to a relative deficiency in ATP, which in turn shifted the mode of cell death toward necrosis. Proximal tubular epithelial cells primarily generate ATP through mitochondrial oxidative phosphorylation, relying heavily on β-oxidation of fatty acids as an energy source, with minimal dependence on

glycolysis. In the proximal tubule, a significant portion of solute reabsorption occurs via secondary active transport driven by the Na^+/K^+-ATPase, which requires a substantial amount of ATP.[30] Our metabolic flux analysis using the Seahorse assay revealed that puberulic acid disrupts mitochondrial respiration, further supporting this mechanism of ATP depletion. When proximal tubular cells are injured and mitochondrial dysfunction impairs energy production, ATP depletion ensues, resulting in characteristic features of Fanconi syndrome may emerge, including glucosuria, aminoaciduria, phosphaturia, bicarbonate loss leading to metabolic acidosis, and low molecular weight proteinuria.[31] This is highly consistent with the Fanconi syndrome-like manifestations observed in both humans and mice following treatment with puberulic acid and *Choleste-Help*. In the future, we plan to investigate the detailed mechanisms of puberulic acid, including its uptake pathways and long-term effects.

In summary, we are the first to demonstrate that puberulic acid and *Choleste-Help* exhibit the same type of toxicity, which is predominantly necrosis. We also showed that mitochondrial dysfunction precedes and likely contributes to this toxicity as one of its key mechanisms. We hope that future studies building on this work will contribute to improving the prognosis and treatment of patients suffering from such toxic effects.

Disclosure Statement

The authors declare that they have no conflicts of interest.

Data Statement

The data that support the findings of this study are available from the corresponding author upon reasonable request. Requests for resources and reagents should be directed to the Lead Contact, Yutaro Mori (y-mori.kid@tmd.ac.jp).

Acknowledgment

We are deeply grateful to the generous study participants who agreed to donate segments of their resected kidneys for this research. This work was supported by Leading Initiative for Excellent Young Researchers (LEADER) from Ministry of Education, Culture, Sports, Science and Technology (to Y.M.), Grant-in-Aid for Research Activity Start-up (22K20881) and Grand-in-Aid for Scientific Research (B) (24K03249) from Japan Society for the Promotion of Science (to Y.M.), Innovation Idea Contest from Tokyo Medical and Dental University (TMDU) (in 2022 to Y.M. and in 2023 to Y.N.), Next Generation Researcher Training Unit from TMDU (to Y.M.) and Priority Research Areas Grant from TMDU (to Y.M.), Research Grant from Uehara Memorial Foundation (to Y.M.), Research Grant (Lifestyle-related diseases) from MSD Life Science Foundation (to Y.M.), Medical Research Grant from Takeda Science Foundation (to Y.M.), Academic Support from Bayer Yakuhin, Ltd. (to Y.M.), and Japan Agency for Medical Research and Development (AMED) (24gm6910017h0001) (to E.S.).

Author contributions

YS performed the experiments, collected and analyzed data, developed experimental strategy and prepared the manuscript. MM supported the experiments. HM, WS and DT obtained human kidney biopsy samples from patients. YS, YM, YN and MM established the hRPTECs and SM helped with the procedure. HK, FA, KS, TM, ES, and SU supported the data analysis. YW, SY, and YF resected the patients' kidneys as standard treatment for malignant diseases. YM supervised the project, modified experimental strategy and finalized the manuscript. All authors discussed the results and implications and provided comments on the manuscript.

Figure Legends

Figure 1. A human kidney biopsy sample of a *Choleste-Help* nephropathy patient show renal tubular injury and necrosis and surrounded interstitial fibrosis.

(a) A HE staining on a human *Choleste-Help* nephropathy kidney. A scale bar: 200 μm.

(b) An immunostaining of KIM-1 and α-SMA on a *Choleste-Help* nephropathy kidney. Scale bars: 100 μm.

Figure 2. Wild type mice showed acute kidney failure and Fanconi-like phenotype by *Choleste-Help* toxic lot and puberulic acid.

(a) Schematic overview of animal experiments treated with *Choleste-Help* toxic lot or puberulic acid.

(b) Blood urea nitrogen (BUN), serum creatinine (Cr), urinary albumin (U-Alb/U-Cr), urinary glucose (U-Glu/U-Cr) and urinary N-acetyl-β-D-glucosaminidase (U-NAG/U-Cr) of mice treated with PBS control, *Choleste-Help* normal lot, toxic lot or puberulic acid (PA). n = 10 for control and for *Choleste-Help* normal lot, n = 9 for toxic lot and n = 6 for puberulic acid. P-values for each comparison are as follows**: BUN**: 0.99 (Control vs Normal Lot), 0.0025 (Normal Lot vs Toxic Lot), 0.003 (Control vs Puberulic acid). **Creatinine**: 0.99 (Control vs Normal Lot), 0.0042 (Normal Lot vs Toxic Lot), < 0.0001 (Control vs Puberulic acid). **U-Alb/U-Cr**: >0.99 (Control vs Normal Lot), 0.0007 (Normal Lot vs Toxic Lot), < 0.0001 (Control vs Puberulic acid). **U-Glu/U-Cr**: >0.99 (Control vs Normal Lot), 0.0006 (Normal Lot vs. Toxic Lot), 0.0137 (Control vs. Puberulic acid). **U-NAG/U-Cr**: 0.99 (Control vs Normal Lot), 0.0666 (Normal Lot vs Toxic Lot), 0.0014 (Control vs Puberulic acid).

(c) HE stainings on mouse kidneys of PBS control (vehicle), *Choleste-Help* normal lot, toxic lot and pubeluric acid. Scale bars: 200 μm.

(d) Masson's Trichrome Stainings and statistical analysis of fibrotic areas on mouse kidneys PBS control (vehicle), *Choleste-Help* normal lot, toxic lot (n = 8, 2 samples without kidney damage excluded) and pubeluric acid. Scale bars: 200 μm.

Figure 3. Mice treated with *Choleste-Help* toxic lot and puberulic acid exhibited highly similar gene expression profiles, as revealed by RNA-seq analysis.

(a) Principal component analysis (PCA) of RNA-seq samples. PCA was performed using rlog-transformed gene expression values. Each point represents one biological replicate. Samples are color-coded by treatment group: control (orange), normal lot (green), toxic lot (blue), and puberulic acid (magenta). PC1 and PC2 explain 86% and 4% of the total variance, respectively.

(b) Hierarchical clustering of RNA-seq samples. Samples were clustered based on Euclidean distance calculated from rlog-transformed gene expression values. Clustering was performed using complete linkage, and the resulting dendrogram illustrates the similarity of global transcriptomic profiles across the four treatment groups: control, normal lot, toxic lot, and puberulic acid. The x-axis labels represent individual biological replicates. Shorter branch lengths indicate greater similarity in expression profiles.

(c) Heatmap of the top 30 differentially expressed genes (DEGs) across treatment conditions. Row-scaled expression levels (Z-scores) of normalized RNA-seq counts are shown for the 30 most significant DEGs (padj < 0.05, |log2 fold change| > 1, baseMean > 10). Each row represents a gene, and each column corresponds to a biological replicate. Samples are annotated by treatment group: control (green), normal lot (blue), toxic lot (orange), and puberulic acid

(magenta). Both genes and samples were hierarchically clustered using Euclidean distance and complete linkage. Color scale indicates standardized expression values (Z-scores), with red representing higher expression and blue representing lower expression relative to the mean of each gene.

(d) Volcano plot of differentially expressed genes between the toxic and normal lots. Each dot represents a gene, with red and blue indicating significantly upregulated and downregulated genes, respectively (adjusted p-value < 0.05 and |log2 fold change| > 1, baseMean > 10). Gray points represent genes with no significant change. The top 10 upregulated and downregulated genes were labeled based on adjusted p-value ranking. For improved visualization, genes with extreme fold changes (|log2FC| > 10, n = 6) were excluded from the plot. The total number of significantly changed genes is indicated in the figure.

(e) Correlation of gene expression fold changes between treatment comparisons. Each point represents a gene, with its log2 fold change (log2FC) in normal lot vs toxic lot (x-axis) and puberulic acid vs control (y-axis). A Pearson correlation coefficient was 0.733. The red dashed line represents a linear regression fit.

(f) Venn diagram showing the overlap of differentially expressed genes (DEGs) between puberulic acid vs control and toxic lot vs normal lot. DEGs were defined by padj < 0.05, |log2FC| > 1, and baseMean > 10. A total of 4144 genes were shared between the two comparisons, accounting for 63.8% of the union set.

Figure 4. Mitochondrial function was significantly suppressed indicated by comprehensive transcriptomic analysis with RNA-seq

(a) GO Cellular Component (CC) enrichment analysis of downregulated genes. Dot plots showing the top 10 significantly enriched GO terms (padj < 0.05) among genes that were downregulated (log2FC < -1, baseMean > 10). The x-axis represents the Gene Ratio (the proportion of input genes associated with each term). The color gradient reflects the adjusted p-value (Benjamini-Hochberg correction), where red indicates higher significance. Bubble size corresponds to the number of genes enriched in each term.

(b) GO-Biological Process enrichment of downregulated genes. Dot plot showing the top 10 significantly enriched GO terms (padj < 0.05) among genes that were downregulated (log2FC < -1, baseMean > 10). The x-axis represents the Gene Ratio (the proportion of input genes associated with each term). The color gradient reflects the adjusted p-value (Benjamini-Hochberg correction), where red indicates higher significance. Bubble size corresponds to the number of genes enriched in each term.

(c) GO-Molecular Function enrichment of downregulated genes. Dot plot showing the top 10 significantly enriched molecular function (MF) terms (padj < 0.05) among genes downregulated (log2FC < -1, baseMean > 10). The x-axis represents the Gene Ratio, defined as the proportion of input genes annotated to each GO term. Dot size indicates the gene count, while dot color represents the adjusted p-value.

Figure 5. Puberulic acid exhibited approximately half the cytotoxicity of cisplatin in hRPTECs and a kidney injury marker and a DNA damage marker were upregulated following puberulic acid exposure.

(a) Cell viability of hRPTECs treated with puberulic acid or cisplatin. n = 9 for each condition. P-values compared with the control were 0.99, 0.0048, and <0.0001 for the 50 μM, 100 μM, and

200 μM Puberulic acid groups, and 0.049, 0.0014, and <0.0001 for the 25 μM, 50 μM, and 100 μM Cisplatin groups, respectively. EC□□ was estimated using a 4-parameter logistic model (see Methods).

(b) Representative western blotting images of γH2AX and Erk1/2 as a loading control from lysate of puberulic acid-treated hRPTECs. Graphs represent densitometric values of each band normalized to the corresponding internal control. P-values for γH2AX were 0.85 (0 μM vs 2.5 μM), <0.0001 (2.5 μM vs 5 μM), and <0.0001 (0 μM vs 5 μM). Full blot images are shown in **Supplementary Figure 10**.

(c) Representative western blotting images of γH2AX, KIM-1 and Erk1/2 as a loading control from lysate of puberulic acid-treated human kidney-derived tubuloids. Graphs represent densitometric values of each band normalized to the corresponding internal control. P-values for γH2AX were 0.65 (0 μM vs 2.5 μM), 0.028 (2.5 μM vs 5 μM), and 0.010 (0 μM vs 5 μM). For Kim-1, P-values were 0.76 (0 μM vs 2.5 μM), 0.99 (2.5 μM vs 5 μM), and 0.80 (0 μM vs 5 μM). Full blot images are shown in **Supplementary Figure 11**.

Figure 6. Necrosis accounted for most of the cell death of hRPTECs treated with puberulic acid.

(a) Representative plots of flow cytometry on hRPTECs treated with puberulic acid or cisplatin stained with Annexin V and propidium iodide (PI) as Annexin V assay. The graph shows the fold change in early apoptosis (Annexin V positive, PI negative) and late apoptosis/necrosis (Annexin V positive, PI positive), normalized to the control group. Independent experiments were conducted three times for both the cisplatin group (n = 3) and the puberulic acid group (n = 5). Statistical analyses were performed on raw (non-normalized) data, and the results were

reflected in the corresponding graphs. In the Cisplatin group, P-values for Early Apoptosis were 0.95 (0 μM vs 25 μM) and 0.0001 (0 μM vs 50 μM), P-values for Late Apoptosis and Necrosis were 0.86 (0 μM vs 25 μM) and <0.0001 (0 μM vs 50 μM). In the Puberulic Acid group, P-values for Early Apoptosis were 0.98 (0 μM vs 50 μM) and 0.020 (0 μM vs 100 μM), P-values for Late Apoptosis and Necrosis were 0.16 (0 μM vs 50 μM) and <0.0001 (0 μM vs 100 μM).

(b) Representative plots of flow cytometry on hRPTECs treated with 100 μM puberulic acid measuring time course of cell death. The graph shows the fold change in early apoptosis (Annexin V positive, PI negative) and late apoptosis/necrosis (Annexin V positive, PI positive), normalized to the control group. Independent experiments were performed twice for both the 24-hour group (n = 3) and the 40-hour group (n = 2). Statistical analyses were performed on raw (non-normalized) data, and the results were reflected in the corresponding graphs. P-values for Early Apoptosis were 0.98 (0 μM vs 50 μM) and 0.020 (0 μM vs 100 μM), P-values for Late Apoptosis and Necrosis were 0.16 (0 μM vs 50 μM) and <0.0001 (0 μM vs 100 μM).

Figure 7. A decrease in mitochondrial membrane potential and ATP deficiency precedes the onset of cell death.

(a) JC-1 staining of hRPTECs treated with puberulic acid and statistical analysis of red/green ratio. Red color indicates J-aggregate and green color indicates JC-1 monomer. n = 18 in each condition. P-values for were 0.0006 (Control vs 18h), <0.0001 (Contorl vs 24h), <0.0001 (Contorl vs 40h) and <0.0001 (Control vs 48h).

(b) ATP levels were measured and normalized to the respective control group at each time point. The values at 0 h represent theoretical references. n = 9 for each. statistical test: Kruskal–Wallis. P-values were 0.45 (Control vs 6h) , 0.012 (Contorl vs 24h) and <0.0001 (Control vs 48h).

Figure 8. Mitochondrial respiration was suppressed following puberulic acid treatment.

(a) Oxygen consumption rate (OCR) was measured in control cells and cells treated with puberulic acid for 4.5 or 9 hours using the Seahorse XF Cell Mito Stress Test. Each point represents the mean ± SEM of six technical replicates. Statistical analysis was performed on the ratio of maximal respiration to basal respiration (Maximal OCR / Basal OCR) to account for potential differences in cell number and to evaluate mitochondrial respiratory capacity in a normalized manner. One replicate in the 9 h treatment group was identified as an outlier (Z-score > 2) and was excluded from the statistical analysis. Puberulic acid reduced maximal respiration in a time-dependent manner, indicating progressive mitochondrial dysfunction. P-values were 0.0004 (Control vs 4.5h), <0.0001(Contorl vs 9h).

(b) Extracellular acidification rates (ECARs) in control and puberulic acid–treated cells were measured using the Seahorse XF Cell Mito Stress Test in control cells and cells treated with puberulic acid for 4.5 or 9 hours. Oligomycin, FCCP, and rotenone/antimycin A were sequentially injected at the indicated time points. Both puberulic acid groups exhibited elevated ECAR after oligomycin injection compared to the control group. Statistical analysis revealed a significant increase in ECAR at the post-oligomycin peak, suggesting a compensatory enhancement of glycolytic activity in response to mitochondrial inhibition. Data are presented as mean ± SEM (n = 6 wells per group). P-values were 0.0007 (Control vs 4.5h), 0.0008(Contorl vs 9h).

References

1 Gabardi, S., Munz, K. & Ulbricht, C. A review of dietary supplement-induced renal dysfunction. *Clin J Am Soc Nephrol* **2**, 757-765 (2007). https://doi.org/10.2215/cjn.00500107

2 Knapik, J. J., Trone, D. W., Steelman, R. A., Farina, E. K. & Lieberman, H. R. Adverse effects associated with use of specific dietary supplements: The US Military Dietary Supplement Use Study. *Food Chem Toxicol* **161**, 112840 (2022). https://doi.org/10.1016/j.fct.2022.112840

3 LaW, M. o. H. *Information on Adverse Events associated with Beni-koji (Red Yeast Rice) related Products.*, <https://www.mhlw.go.jp/stf/seisakunitsuite/bunya/kenkou_iryou/shokuhin/daietto/index_00005.html> (2024).

4 Higa, Y. *et al.* Divergence of metabolites in three phylogenetically close Monascus species (M. pilosus, M. ruber, and M. purpureus) based on secondary metabolite biosynthetic gene clusters. *BMC Genomics* **21**, 679 (2020). https://doi.org/10.1186/s12864-020-06864-9

5 Fukami, H. *et al.* A Review of Red Yeast Rice, a Traditional Fermented Food in Japan and East Asia: Its Characteristic Ingredients and Application in the Maintenance and Improvement of Health in Lipid Metabolism and the Circulatory System. *Molecules* **26** (2021). https://doi.org/10.3390/molecules26061619

6 Maiguma, M. *et al.* Successful treatment of acute tubulointerstitial nephritis probably due to Benikoji CholesteHelp(®), a supplement containing red yeast rice. *CEN Case Rep* **14**, 24-28 (2025). https://doi.org/10.1007/s13730-024-00897-9

7 Maruyama, H. *et al.* Successful Resolution of Suspected Red Yeast Rice-induced Nephropathy. *Intern Med* (2025). https://doi.org/10.2169/internalmedicine.4908-24

8 Miyazaki, R. *et al.* Acute kidney tubular injury after ingestion of red yeast rice supplement. *Clin Kidney J* **17**, sfae151 (2024). https://doi.org/10.1093/ckj/sfae151

9 Shinzawa, M. *et al.* A nationwide questionnaire study evaluated kidney injury associated with Beni-koji tablets in Japan. *Kidney Int* **107**, 530-540 (2025). https://doi.org/10.1016/j.kint.2024.11.027

10 Tanaka, S. *et al.* Novel compounds isolated from health food products containing beni-koji (red yeast rice) with adverse event reports. *J Nat Med* **78**, 845-848 (2024). https://doi.org/10.1007/s11418-024-01827-w

11 Yoshinari, T. *et al.* Mechanism of puberulic acid contamination in red yeast rice tablets that caused a serious food poisoning outbreak in Japan. *Proc Jpn Acad Ser B Phys Biol Sci* (2025). https://doi.org/10.2183/pjab.101.017

12 Nakanoh, H. *et al.* Development and Validation of a Stem Cell–Based Kidney Organoid Platform for Nephrotoxicity Assessment. *medRxiv*, 2025.2004.2030.651410 (2025). https://doi.org/10.1101/2025.04.30.651410

13 Nakanoh, H. *et al.* in *Am J Nephrol* 1-9 (© 2025 The Author(s). Published by S. Karger AG, Basel., 2025).

14 Iwatsuki, M. *et al.* In vitro and in vivo antimalarial activity of puberulic acid and its new analogs, viticolins A-C, produced by Penicillium sp. FKI-4410. *J Antibiot (Tokyo)* **64**, 183-188 (2011). https://doi.org/10.1038/ja.2010.124

15 Lukinich-Gruia, A. T. *et al.* Aristolochic acid I as an emerging biogenic contaminant involved in chronic kidney diseases: A comprehensive review on exposure pathways, environmental health issues and future challenges. *Chemosphere* **297**, 134111 (2022). https://doi.org/10.1016/j.chemosphere.2022.134111

16 Cui, T. *et al.* Clinical and safety outcomes associated with aristolochic acid exposure: a systematic review and meta-analysis. *Toxicol Mech Methods*, 1-11 (2025). https://doi.org/10.1080/15376516.2025.2457340

17 Li, C. *et al.* Unveiling correlations between aristolochic acids and liver cancer: spatiotemporal heterogeneity phenomenon. *Chin Med* **19**, 132 (2024). https://doi.org/10.1186/s13020-024-01003-y

18 Ichimura, T. *et al.* Kidney injury molecule-1 is a phosphatidylserine receptor that confers a phagocytic phenotype on epithelial cells. *The Journal of clinical investigation* **118**, 1657-1668 (2008). https://doi.org/10.1172/jci34487

19 Mori, Y. *et al.* KIM-1 mediates fatty acid uptake by renal tubular cells to promote progressive diabetic kidney disease. *Cell Metab* **33**, 1042-1061.e1047 (2021). https://doi.org/10.1016/j.cmet.2021.04.004

20 Ichimura, T. *et al.* Kidney injury molecule-1 (KIM-1), a putative epithelial cell adhesion molecule containing a novel immunoglobulin domain, is up-regulated in renal cells after injury. *The Journal of biological chemistry* **273**, 4135-4142 (1998).

21 Yang, L., Besschetnova, T. Y., Brooks, C. R., Shah, J. V. & Bonventre, J. V. Epithelial cell cycle arrest in G2/M mediates kidney fibrosis after injury. *Nat Med* **16**, 535-543, 531p following 143 (2010). https://doi.org/10.1038/nm.2144

22 Ferenbach, D. A. & Bonventre, J. V. Mechanisms of maladaptive repair after AKI leading to accelerated kidney ageing and CKD. *Nat Rev Nephrol* **11**, 264-276 (2015). https://doi.org/10.1038/nrneph.2015.3

23 O'Sullivan, E. D., Hughes, J. & Ferenbach, D. A. Renal Aging: Causes and Consequences. *J Am Soc Nephrol* **28**, 407-420 (2017). https://doi.org/10.1681/ASN.2015121308

24 Anders, H. J. & Schaefer, L. Beyond tissue injury-damage-associated molecular patterns, toll-like receptors, and inflammasomes also drive regeneration and fibrosis. *J Am Soc Nephrol* **25**, 1387-1400 (2014). https://doi.org/10.1681/ASN.2014010117

25 Zhang, Q. *et al.* Circulating mitochondrial DAMPs cause inflammatory responses to injury. *Nature* **464**, 104-107 (2010). https://doi.org/10.1038/nature08780

26 Nicotera, P., Leist, M. & Ferrando-May, E. Intracellular ATP, a switch in the decision between apoptosis and necrosis. *Toxicol Lett* **102-103**, 139-142 (1998). https://doi.org/10.1016/s0378-4274(98)00298-7

27 Zubair, M. & Bokhari, S. R. A. in *StatPearls* (2025).

28 Leist, M., Single, B., Castoldi, A. F., Kuhnle, S. & Nicotera, P. Intracellular adenosine triphosphate (ATP) concentration: a switch in the decision between apoptosis and necrosis. *J Exp Med* **185**, 1481-1486 (1997). https://doi.org/10.1084/jem.185.8.1481

29 Eguchi, Y., Shimizu, S. & Tsujimoto, Y. Intracellular ATP levels determine cell death fate by apoptosis or necrosis. *Cancer Res* **57**, 1835-1840 (1997).

30 Tsuchiya, K., Wang, W., Giebisch, G. & Welling, P. A. ATP is a coupling modulator of parallel Na,K-ATPase-K-channel activity in the renal proximal tubule. *Proc Natl Acad Sci U S A* **89**, 6418-6422 (1992). https://doi.org/10.1073/pnas.89.14.6418

31 Forst, A. L., Reichold, M., Kleta, R. & Warth, R. Distinct Mitochondrial Pathologies Caused by Mutations of the Proximal Tubular Enzymes EHHADH and GATM. *Front Physiol* **12**, 715485 (2021). https://doi.org/10.3389/fphys.2021.715485

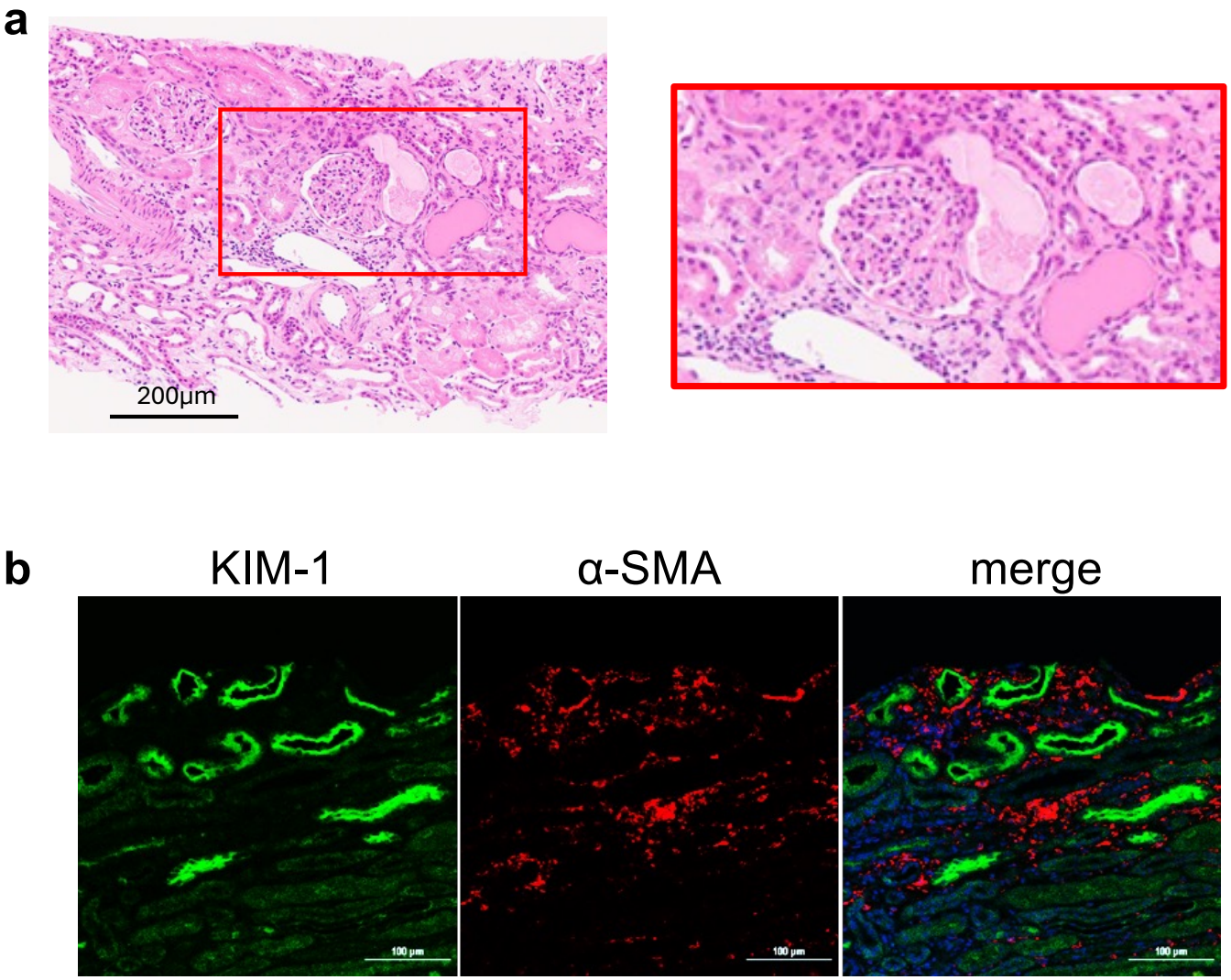

Figure 1

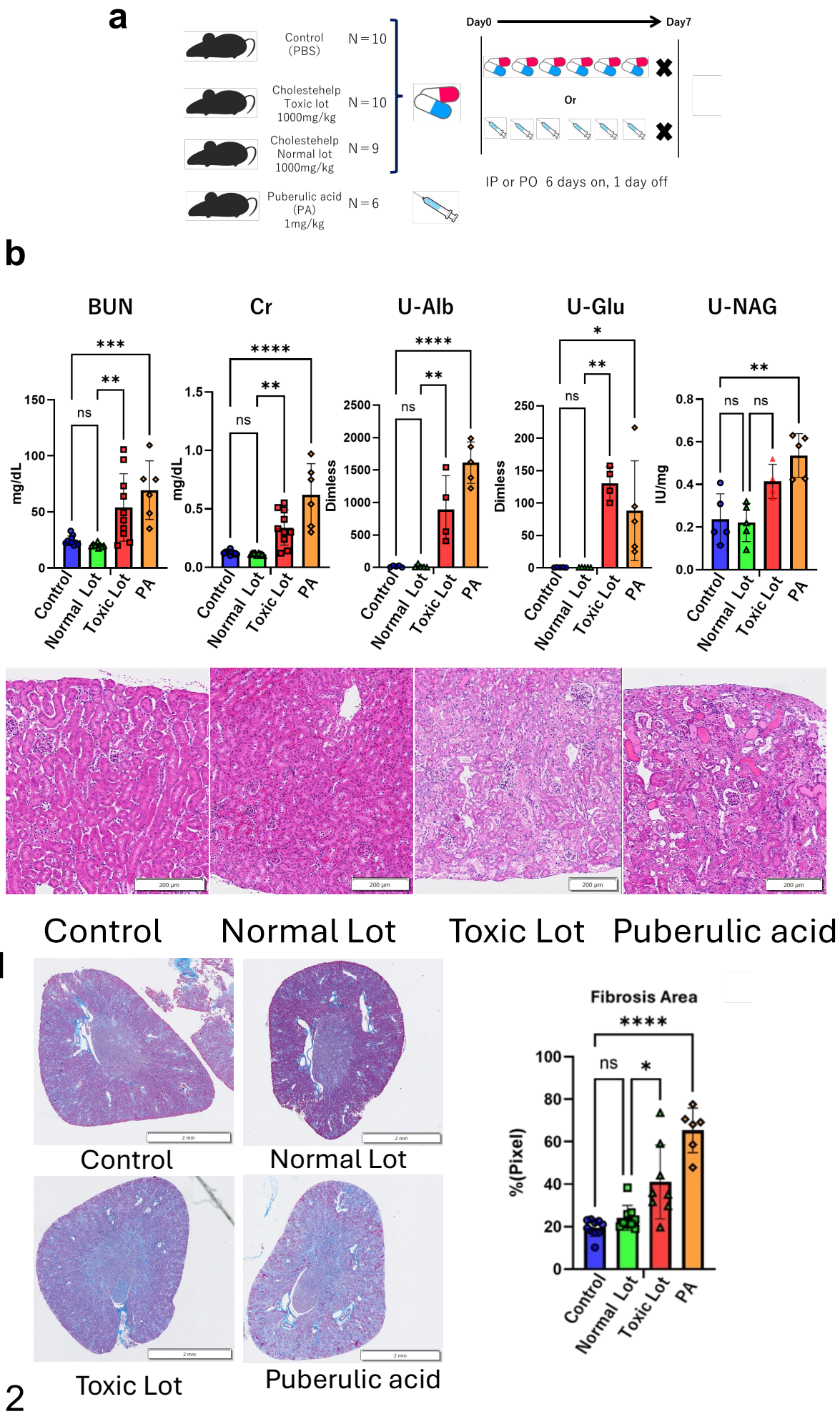
a
Control (PBS)
N = 10
Cholestehelp Toxic lot 1000mg/kg
N = 10
Cholestehelp Normal lot 1000mg/kg
N = 9
Puberulic acid (PA) 1mg/kg
N = 6
Day0
Day7
Or
IP or PO 6 days on, 1 day off
b
BUN
Cr
U-Alb
U-Glu
U-NAG
mg/dL
Dimless
IU/mg
ns
**
***
****
*
Control
Normal Lot
Toxic Lot
PA
c
200 μm
Control
Normal Lot
Toxic Lot
Puberulic acid
d
2 mm
Control
Normal Lot
Toxic Lot
Puberulic acid
Fibrosis Area
%(Pixel)

Figure 2

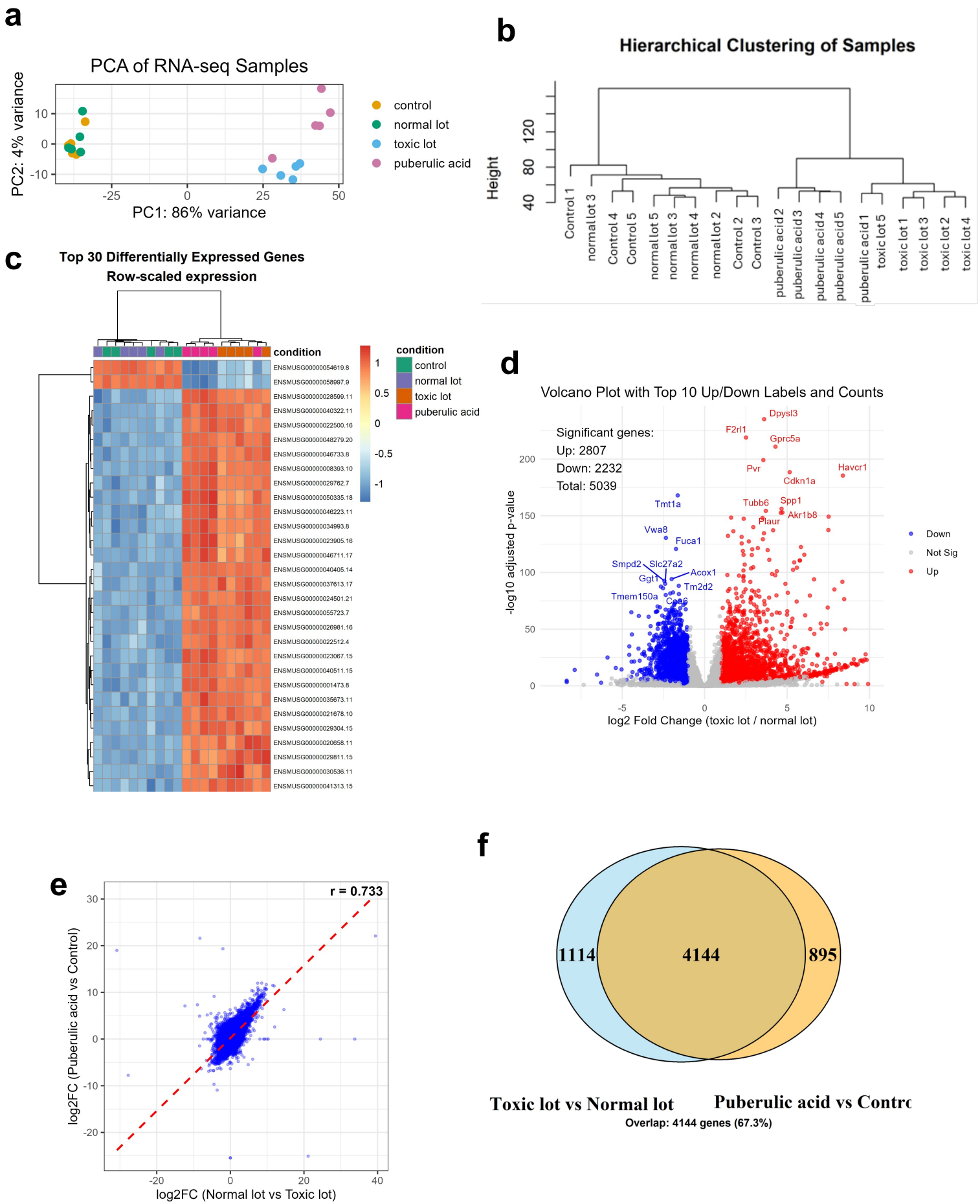
a
PCA of RNA-seq Samples
PC2: 4% variance
PC1: 86% variance
control
normal lot
toxic lot
puberulic acid
b
Hierarchical Clustering of Samples
Height
Control 1
normal lot 3
Control 4
Control 5
normal lot 5
normal lot 3
normal lot 4
normal lot 2
Control 2
Control 3
puberulic acid 2
puberulic acid 3
puberulic acid 4
puberulic acid 5
puberulic acid 1
toxic lot 5
toxic lot 1
toxic lot 3
toxic lot 2
toxic lot 4
c
Top 30 Differentially Expressed Genes
Row-scaled expression
condition
control
normal lot
toxic lot
puberulic acid
d
Volcano Plot with Top 10 Up/Down Labels and Counts
Significant genes:
Up: 2807
Down: 2232
Total: 5039
Dpysl3
F2rl1
Gprc5a
Pvr
Havcr1
Cdkn1a
Tmt1a
Tubb6
Spp1
Akr1b8
Plaur
Vwa8
Fuca1
Smpd2
Slc27a2
Acox1
Ggt1
Tm2d2
Tmem150a
Down
Not Sig
Up
-log10 adjusted p-value
log2 Fold Change (toxic lot / normal lot)
e
r = 0.733
log2FC (Puberulic acid vs Control)
log2FC (Normal lot vs Toxic lot)
f
1114
4144
895
Toxic lot vs Normal lot
Puberulic acid vs Contro
Overlap: 4144 genes (67.3%)

Figure 3

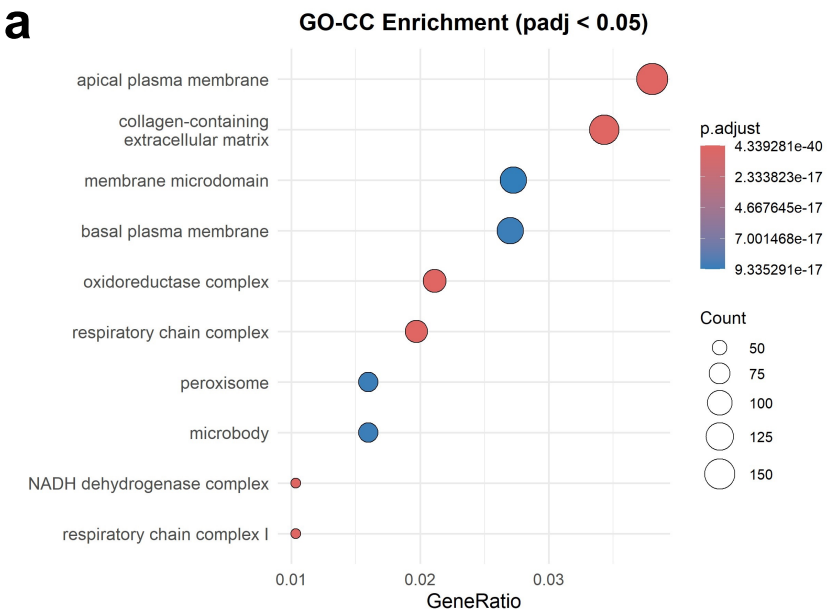
a
GO-CC Enrichment (padj < 0.05)
apical plasma membrane
collagen-containing extracellular matrix
membrane microdomain
basal plasma membrane
oxidoreductase complex
respiratory chain complex
peroxisome
microbody
NADH dehydrogenase complex
respiratory chain complex I
0.01
0.02
0.03
GeneRatio
p.adjust
4.339281e-40
2.333823e-17
4.667645e-17
7.001468e-17
9.335291e-17
Count
50
75
100
125
150

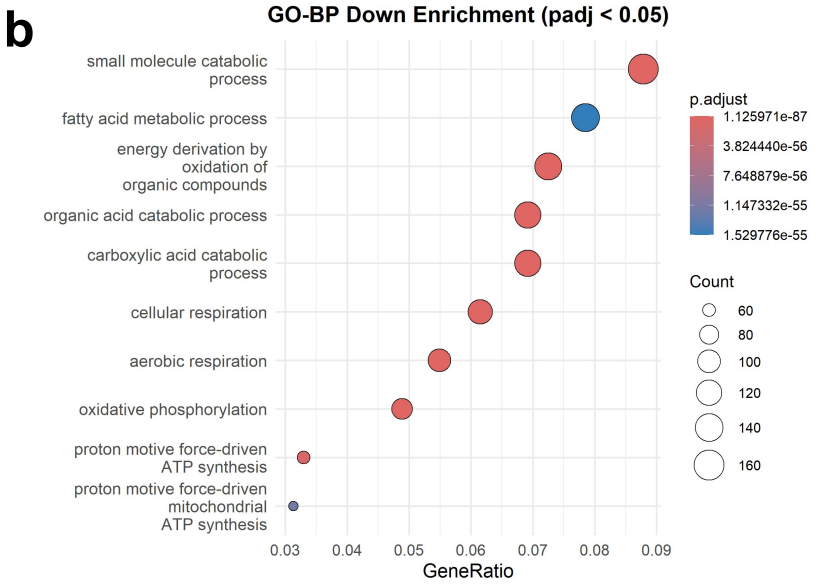
b
GO-BP Down Enrichment (padj < 0.05)
small molecule catabolic process
fatty acid metabolic process
energy derivation by oxidation of organic compounds
organic acid catabolic process
carboxylic acid catabolic process
cellular respiration
aerobic respiration
oxidative phosphorylation
proton motive force-driven ATP synthesis
proton motive force-driven mitochondrial ATP synthesis
0.03
0.04
0.05
0.06
0.07
0.08
0.09
GeneRatio
p.adjust
1.125971e-87
3.824440e-56
7.648879e-56
1.147332e-55
1.529776e-55
Count
60
80
100
120
140
160

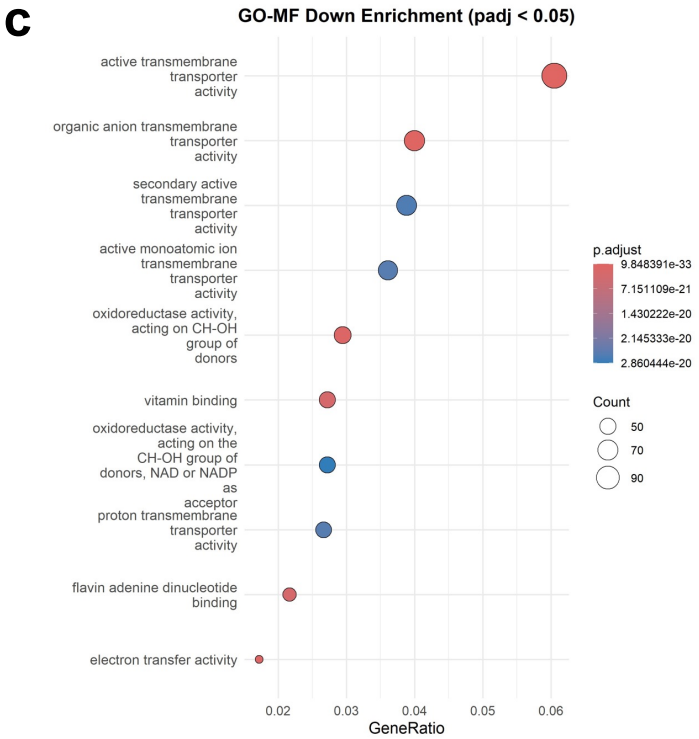
c
GO-MF Down Enrichment (padj < 0.05)
active transmembrane transporter activity
organic anion transmembrane transporter activity
secondary active transmembrane transporter activity
active monoatomic ion transmembrane transporter activity
oxidoreductase activity, acting on CH-OH group of donors
vitamin binding
oxidoreductase activity, acting on the CH-OH group of donors, NAD or NADP as acceptor
proton transmembrane transporter activity
flavin adenine dinucleotide binding
electron transfer activity
0.02
0.03
0.04
0.05
0.06
GeneRatio
p.adjust
9.848391e-33
7.151109e-21
1.430222e-20
2.145333e-20
2.860444e-20
Count
50
70
90

Figure 4

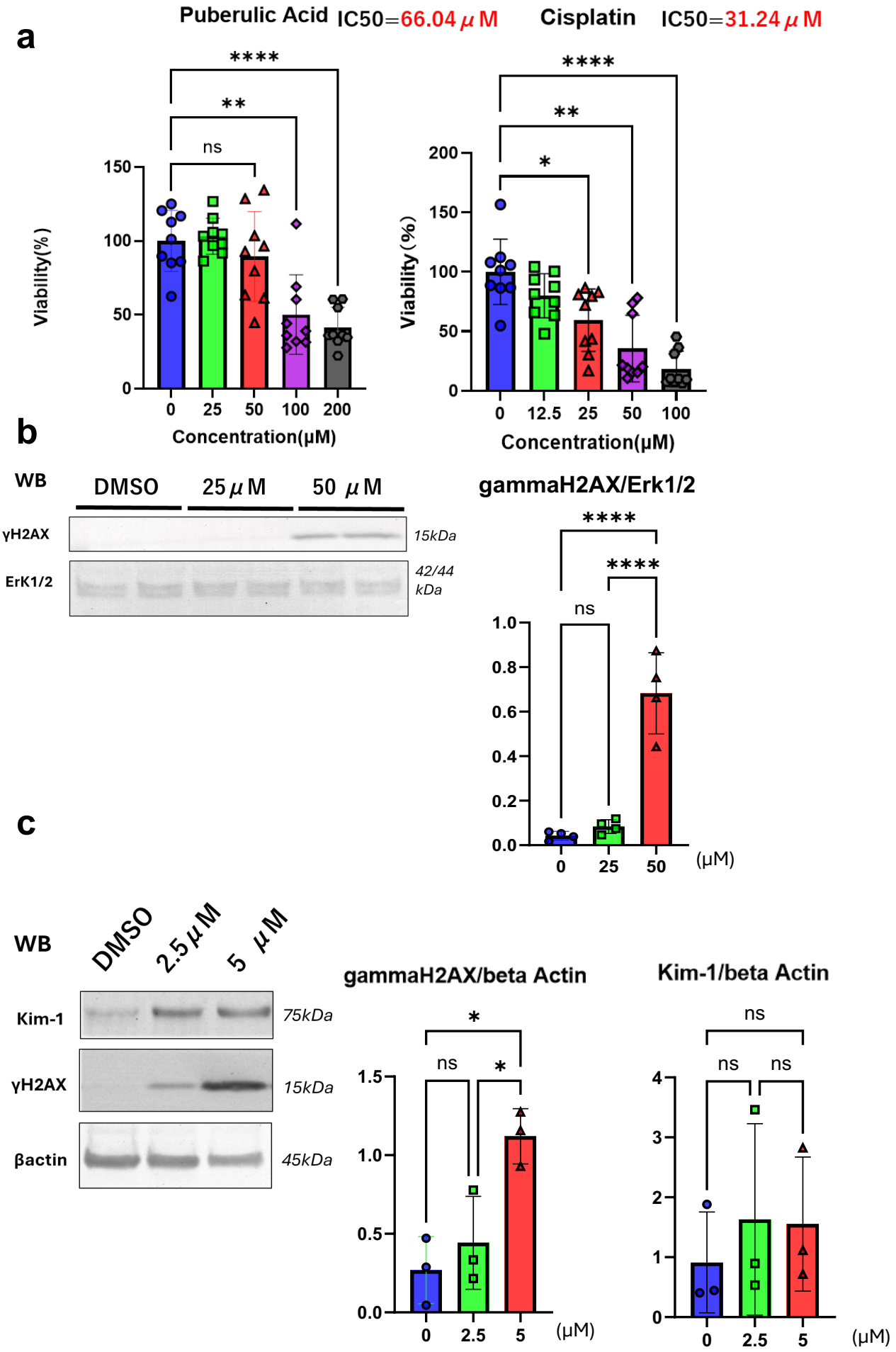
a
Puberulic Acid IC50=66.04 μM
Cisplatin IC50=31.24 μM
****
**
ns
*
Viability(%)
Concentration(μM)
b
WB
DMSO
25 μM
50 μM
γH2AX
ErK1/2
15kDa
42/44 kDa
gammaH2AX/Erk1/2
(μM)
c
WB
DMSO
2.5 μM
5 μM
Kim-1
γH2AX
βactin
75kDa
15kDa
45kDa
gammaH2AX/beta Actin
Kim-1/beta Actin

Figure 5

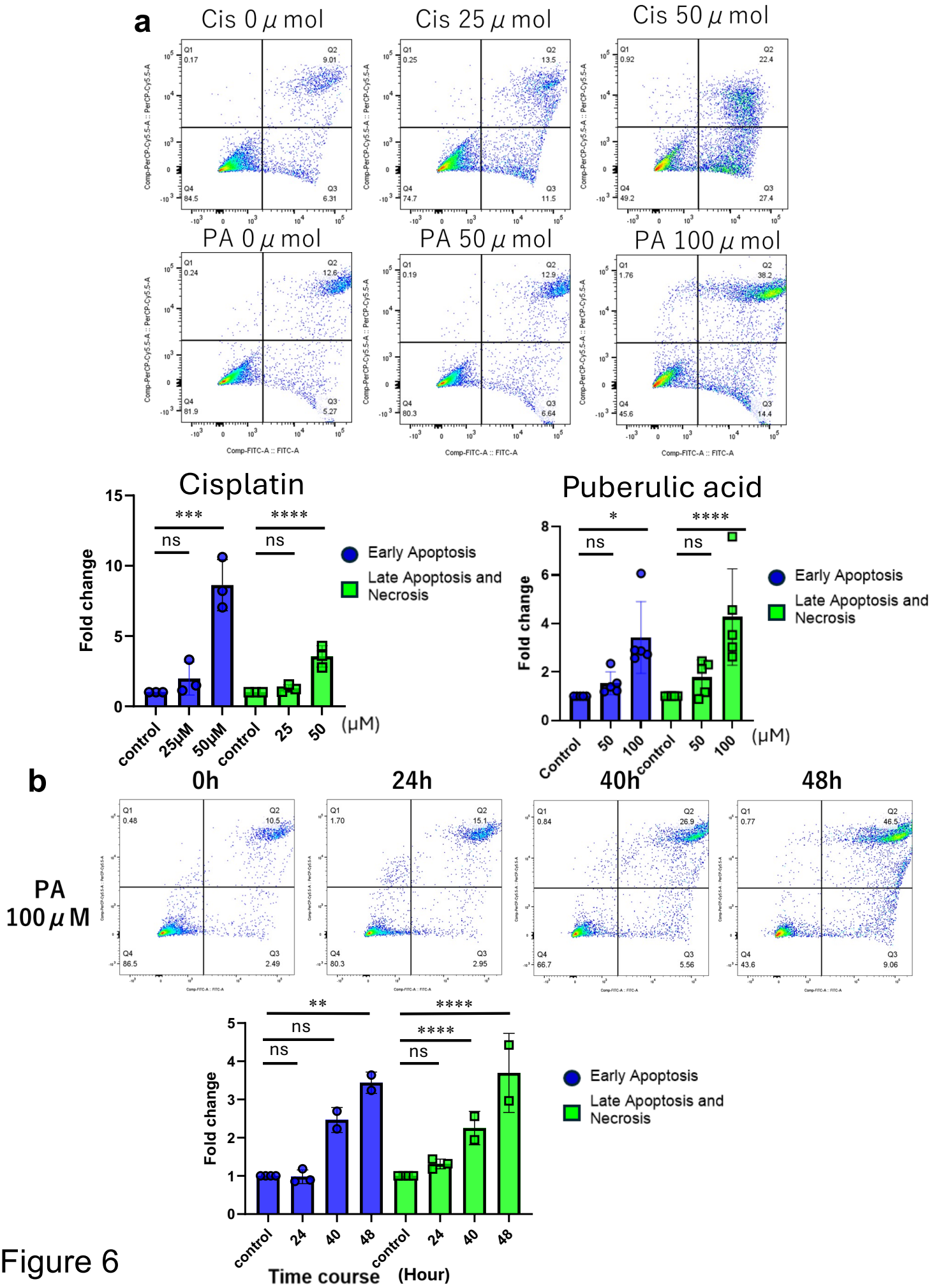
a
Cis 0 μ mol
Cis 25 μ mol
Cis 50 μ mol
PA 0 μ mol
PA 50 μ mol
PA 100 μ mol
Comp-PerCP-Cy5.5-A :: PerCP-Cy5.5-A
Comp-FITC-A :: FITC-A
Cisplatin
Puberulic acid
Fold change
Early Apoptosis
Late Apoptosis and Necrosis
control
25μM
50μM
25
50
100
(μM)
b
PA 100 μ M
0h
24h
40h
48h
Time course (Hour)

Figure 6

a

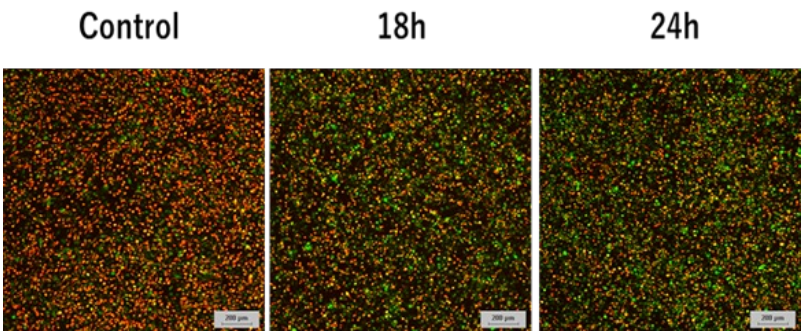
Control
18h
24h

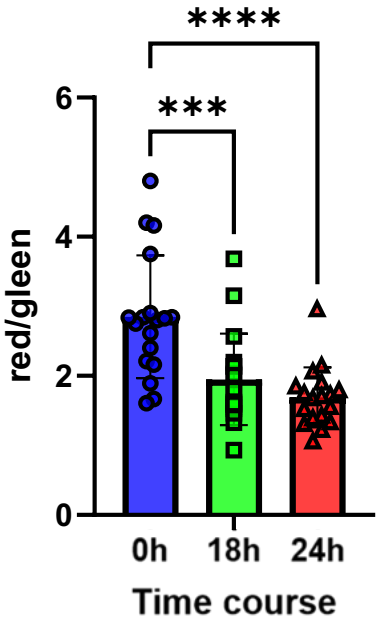
****
***
6
4
2
0
red/gleen
0h
18h
24h
Time course

b

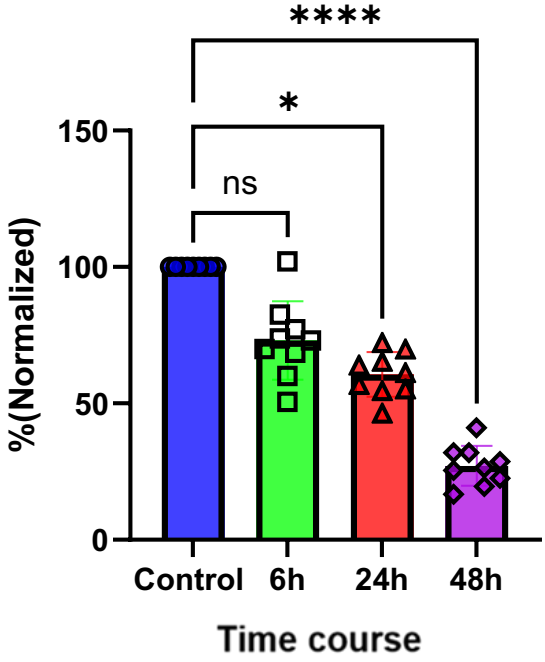
****
*
ns
150
100
50
0
%(Normalized)
Control
6h
24h
48h
Time course

Figure 7

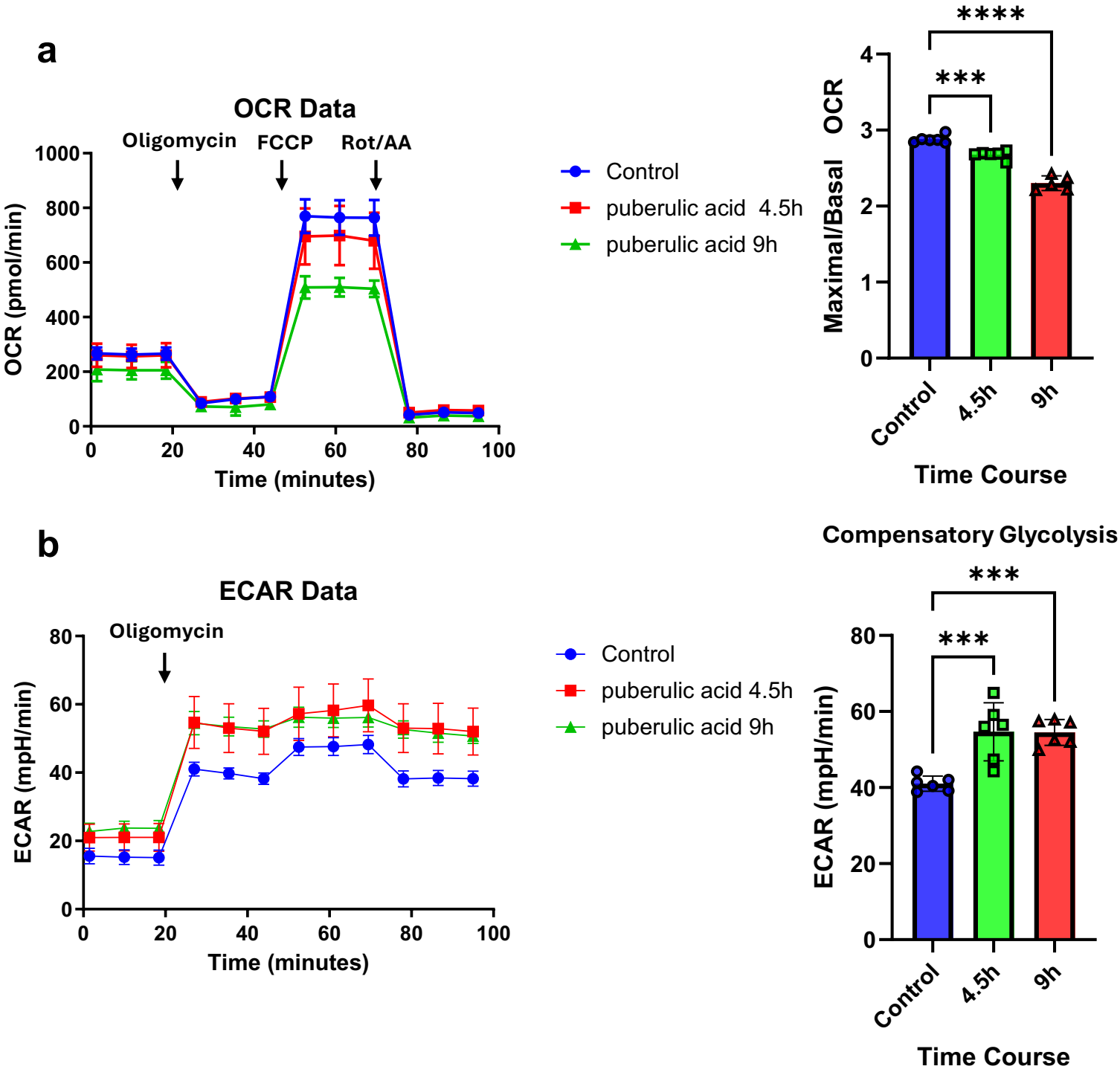
a
OCR Data
Oligomycin
FCCP
Rot/AA
OCR (pmol/min)
Time (minutes)
Control
puberulic acid 4.5h
puberulic acid 9h
Maximal/Basal OCR
****
***
Control
4.5h
9h
Time Course
b
ECAR Data
Oligomycin
ECAR (mpH/min)
Time (minutes)
Control
puberulic acid 4.5h
puberulic acid 9h
Compensatory Glycolysis
***
***
ECAR (mpH/min)
Control
4.5h
9h
Time Course

Figure 8